ORIGINAL PAPER - PRODUCTION GEOPHYSICS

Mechanical behavior and constitutive model of shale under real-time high temperature and high stress conditions

Wuhao Guo[1,2] · Yintong Guo[1] · Zhenhua Cai[3] · Hanzhi Yang[4] · Lei Wang[1] · Chunhe Yang[1,4] · Guokai Zhao[4] ·
Zhenhui Bi[1,2]

Abstract
The high temperature and high in-situ stress geological environment can significantly affect the mechanical properties, failure modes, and deformation characteristics of deep shale reservoirs. In this study, real-time high temperature triaxial compressive tests simulating the deep shale formation environment (temperature: 25–150 °C, confining pressure: 0–100 MPa) are carried out. The GSI-strength degradation and constitutive models are derived based on the Hoek–Brown criterion. The results show that in low confining pressure conditions, the mechanical behavior of shale is greatly influenced by temperature. Compared with shale at 25 °C, the compressive strength of shale at 150 °C decreases by up to 13.7%, and the elastic modulus decreases by up to 36.9%. The peak strain was increased by a factor of up to 1.4, and the yield stress level was advanced by as much as 7.4%. However, in high confining pressure conditions, the shale plasticity characteristics are significantly enhanced and the failure mode is relatively single. The GSI-strength degradation model can well characterize the variation law of shale strength with confining pressure under high temperature conditions. The statistical damage constitutive model matches the actual stress–strain curve very well, and it can fully reflect the deformation and failure characteristics of deep shale. The findings of this study can help us better understand the variation of mechanical properties of deep shale.

Keywords Deep shale · High temperature and high pressure · Rock mechanics · Hoek–Brown criterion · Strength model · Constitutive model

List of symbols

σ_0	Yield stress
σ_1	Maximum effective principal stress
σ_3	Minimum effective principal stress
σ_r	Residual stress
σ^*	Effective stress
ε_0	Yield strain
ε_1	Peak strain
ε_1^*	Effective strain
ε_p	Failure strain
E	Elastic modulus
σ_c	Uniaxial compressive strength
m_b, m_i, s, a	Empirical parameters for different rock masses
T	Temperature
D	Damage variable
N	Total number of micro units
N_d	Accumulated damages of microunits
γ, β	Weibull distribution parameters
I_1^*	First invariant of the effective stress tensor
J_2^*	Second invariant of the partial effective stress tensor

Abbreviations

GSI	Geological intensity index
XRD	X-ray diffraction
LVDT	Linear variable differential transformer

✉ Yintong Guo
  ytguo@whrsm.ac.cn

  Zhenhua Cai
  caizh.cpoe@cnpc.com.cn

1 State Key Laboratory of Geomechanics and Geotechnical Engineering, Institute of Rock and Soil Mechanics, Chinese Academy of Sciences, Wuhan 430071, China

2 University of Chinese Academy of Sciences, Beijing 100049, China

3 CNPC Offshore Engineering Company Limited, Beijing 100176, China

4 State Key Laboratory of Coal Mine Disaster Dynamics and Control, Chongqing University, Chongqing 400044, China

Introduction

Natural gas, as a low-carbon and clean energy source, is indispensable in the process of optimizing and transforming the energy structures of nations around the world (Wang et al. 2017; Al-Fatlawi 2018; Sadeq et al. 2020; Han et al. 2021; Zhang et al. 2022a). Shale gas, as the main source of natural gas and one of the energy sources with the most development potential and excellent potential, makes the global oil and gas industry focus on the unconventional oil and gas fields with huge potential (Long et al. 2018; Liu et al. 2021; Zou et al. 2021; Li et al. 2022). The successful development of shale gas in the Fuling area of China has demonstrated that the development of shale gas would be of considerable significance, with far-reaching demonstration and leadership roles (Liang et al. 2020). On the other hand, the unexploited reserves of deep shale gas (burial depth > 3500 m) are enormous, and efficient deep shale gas development is a critical guarantee for China to achieve energy optimization and transformation (Long et al. 2018; Ma et al. 2021). Therefore, deep shale gas has become the primary target in the Chinese energy exploitation field. However, the large burial depth (> 3500 mm), high formation temperature (> 100 °C), high in-situ stress (> 80 MPa) and high horizontal stress difference (> 25 MPa), are still unavoidable and difficult problems when designing a hydraulic fracturing stimulation plan (Zeng et al. 2016; Jiang et al. 2017; Duan et al. 2019). The deeper the burial depth, the more complex the formation environment is, which makes deep shale and middle-shallow shale show different rock mechanical characteristics. The most obvious point is that the brittle character of deep shale will be significantly reduced. Therefore, to ensure the safety and economy of fracturing stimulation, it has become an urgent scientific problem to explore the rock mechanical properties of deep shale (Fig. 1).

Many scholars have studied the mechanical properties and deformation laws of deep shale. In terms of rock mechanics, Wang et al. (2022) systematically revealed differences in the mechanical behavior of reservoir shale, roof and floor with downhole cores in southern Sichuan, China as the research object. Based on acoustic emission technology, Li (2021) studied the mechanical characteristics of shale under different formation temperatures (20–60 °C) and confining pressures (90–130 MPa), and found that the plastic enhancement of deep shale is one of the important factors for the poor effect of hydraulic fracturing. The findings of Masri et al. (2014) and Mohamadi and Wan (2016) showed that the increase in temperature will reduce the magnitude of the decrease in shale strength and notably affect the deformation ability of shale. Guo et al. (2020) and Fan et al. (2021) found by experiment that the complexity of the rupture surface of shale with bedding plane angles of 0°, 45° and 90° were more sensitive to temperature changes and more prone to strain softening effect. Under thermal-cold shock conditions, Wu et al. (2018) and Guo et al. (2022) evaluated the variation law of rock properties in shallow and deep shale. Yang et al. (2021) carried out the Brazilian splitting test of shale at 600 °C, and the results show that 400 °C is the critical value for the change of shale tensile strength. S. Han et al. and Vishal et al. Vishal et al. (2022) studied
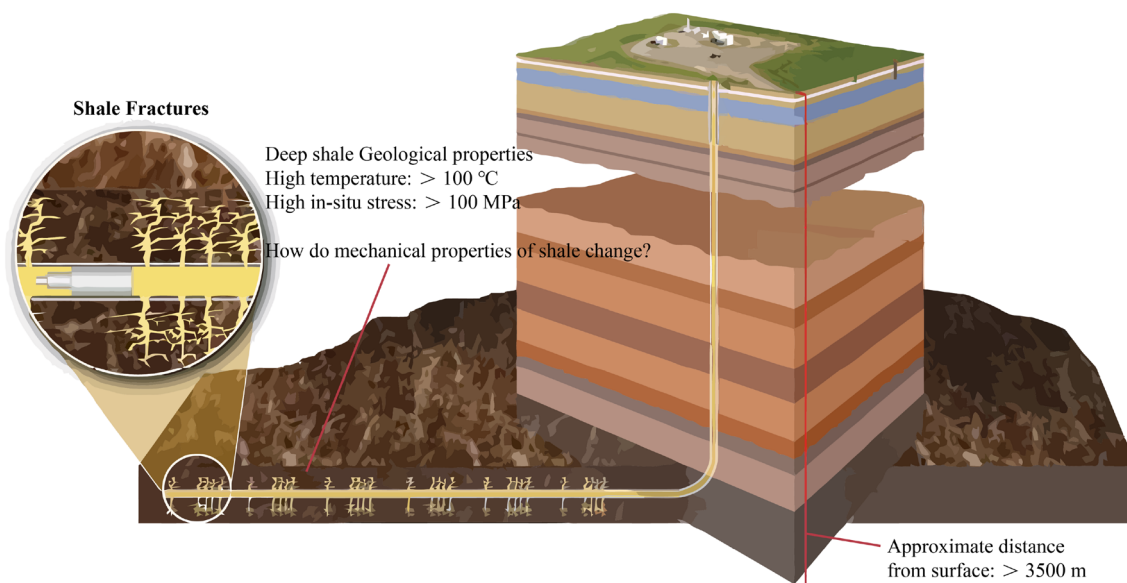
Fig. 1 Geological environment of deep shale (modified from Department of Energy 2012)

the crack propagation mechanism of shale and found that high temperature is conducive to crack propagation. Taking brittleness as the starting point and combining with the triaxial mechanical test of shale, many literature (Liu et al. 2020a; Wan et al. 2022; Yi-Sheng et al. 2022) discussed the elastic–plastic characteristics of shale under different mineral content and the factors of transition from brittleness to ductility. In terms of the rock damage constitutive model, since Lemaitre (Lemaitre 1985) proposed the strain equivalence theory, many scholars have established rock constitutive models suitable for different test conditions on this basis. Qi et al. (2021) established an elastic–plastic constitutive model based on Unified strength theory, which better reflects the rock microporosity compaction phenomenon in the compressive test. Xing et al. (2020) established a high temperature constitutive model for shale based on the Drucker-Prager hardening criterion and extended it to other rock materials. Based on the Drucker-Prager criterion and Weibull distribution, Zhang et al. (2020) derived the constitutive model of sandstone under freezing conditions. Based on the Mohr–Coulomb criterion, Jiang et al. (2021) derived a sandstone constitutive model under the influence of temperature and explained the physical meaning of the parameters in the model. Liu et al. (2018) derived a 4-parameter rock constitutive model based on Maximum tensile strain criterion and proposed a method for estimating the rock elastic modulus. Zhao et al. (2019 and Ye et al. (2022) considered the effect of temperature on the thermal damage of shale, and the proposed intrinsic model can accurately reflect the deformation characteristics of shale at high temperature. In addition, many scholars (Wang et al. 2018; Xu et al. 2018; Liu et al. 2020b, c) have done a lot of research on the constitutive model of thermal damage, all of which reveal the effect of temperature on the deterioration of physical and mechanical properties of rocks. Although the above studies have considerably enriched the development of rock mechanical characteristics and damage evolution laws, none of them has considered the relationship between rock deformation and stress under the action of real-time temperature. When the heat treatment temperature does not reach the rock's threshold temperature, the preheated samples' experimental results do not represent the real mechanical characteristics of the rock under the high temperature formations (Zhang et al. 2022b). In addition, the strength criterion introduced in the above constitutive model has certain limitations (Chen et al. 2021). Therefore, in this paper, real-time high temperature and high stress triaxial compression tests were conducted on the rock mechanics test system for the shale of the Lower Silurian Longmaxi formation. Based on real-time high temperature triaxial compressive test, a GSI-strength degradation model of shale under temperature effect is established. Meanwhile, the statistical damage constitutive model of shale under high temperature and high stress was derived based on the GSI-strength degradation model with the starting point that the strength of rock micro units conformed to the Weibull statistical distribution law, and the model matched the actual test curves to a high degree. The research results can provide certain ideas for solving the problems encountered in deep shale hydraulic fracturing stimulation.

Materials and test system

Sample preparation

The shale outcrops chosen for the test came from Shizhu County (Geographical coordinates: N: 29°39′–30°33′, E: 107°59′–108°34′) in China's Sichuan Basin (Fig. 2a), which is one of the most successful areas for deep shale
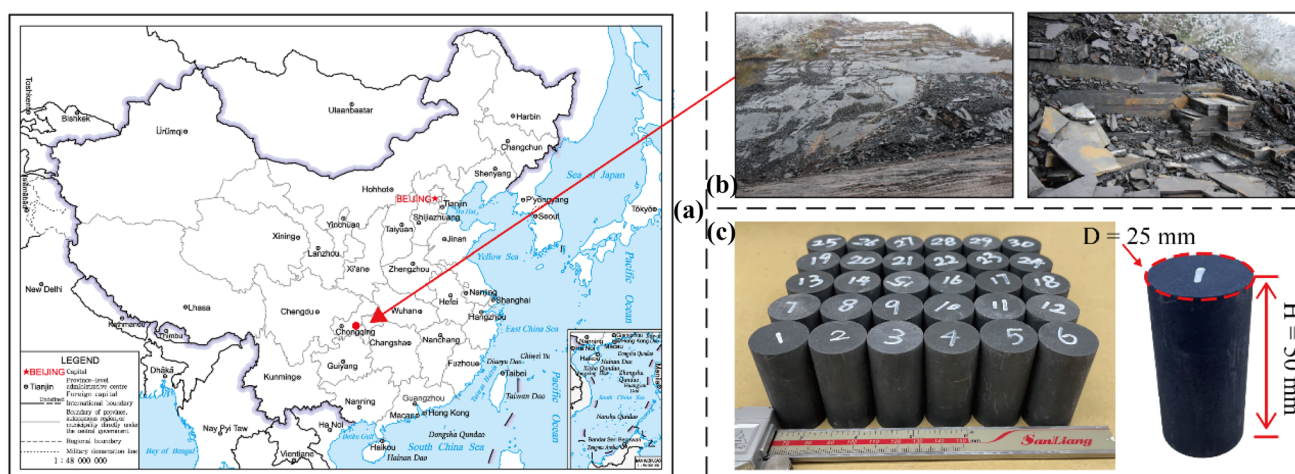

Fig. 2 Sampling Point, Shale landscape and sample preparation

hydraulic fracturing stimulation in China. The shale belongs to the lower Silurian Longmaxi formation in the Fuling area of the Sichuan Basin. From the sampling site (Fig. 2b), the shale bedding in this area is relatively developed, the surface weathering degree of the outcrop is high, making sampling challenging. After stripping the weathering layer from the surface of the shale outcrop, we collected complete shale blocks measuring approximately 600 mm × 400 mm × 400 mm. In the vertical bedding plane direction, we drilled long cylindrical shale using water-inject coring and ground the fragments for X-ray diffraction analysis. According to the sample processing method recommended by ISRM (ISRM 1984), the shale was processed into standard cylindrical shale samples of Φ25 mm × 50 mm (Fig. 2c). Meanwhile, we tested the fundamental physical properties of the processed shale samples and selected samples with similar physical properties for the next step of high temperature triaxial compressive tests (Table 1).

Experimental equipment and procedure

The modified Rock mechanics test system (XTR01-01) of WHRSM, CAS was used to conduct real-time high temperature triaxial compressive tests (Fig. 3a). The maximum heating temperature of the heating module in the test system is 250 °C, and the temperature control accuracy is ± 0.1 °C. The overall stiffness of the frame in the stress loading module is 11GN/m, the ultimate axial load is 2000 kN, and the ultimate confining pressure is 150 MPa. The axial strain sensor is a 6 mm linear variable differential transformer (LVDT), and the radial strain sensor is a circumferential strain gage with a range of 8 mm, both of which have a control accuracy of 1‰ (Fig. 3b). Considering the complex formation environment in deep shales (> 3500 m) (He et al. 2021; Zhang et al. 2022a), the confining pressure and temperature were set to 0–30–60–100 MPa and 25–80–150 °C, respectively.

Table 1 Sample information and fundamental physical properties

Sample no.[a]	Diameter mm	Height mm	Test types	Properties	Mean ± standard deviation
TCS-0-25	25.14	49.94	XRD test	Density (g/cm³)	2.41 ± 0.03
TCS-30-25	25.15	50.02		Permeability (10^{-6} μm^{-2})	0.208 ± 0.126
TCS-60-25	25.15	50.06		Porosity (%)	6.374 ± 1.573
TCS-100-25	24.77	50.04		P-wave velocity (m/s)	4222.9 ± 180.2
TCS-0-80	25.12	50.06			
TCS-30-80	25.15	49.89			
TCS-60-80	25.14	50.08	Triaxial compressive test		
TCS-100-80	25.14	50.01			
TCS-0-150	25.13	50			
TCS-30-150	25.13	49.99			
TCS-60-150	25.15	49.96			
TCS-100-150	25.13	50.06			

[a]TCS-0-25, where 0 represents the confining pressure of 0 MPa and 25 represents the temperature of 25 °C

**Fig. 3** Rock mechanics test system and strain sensor
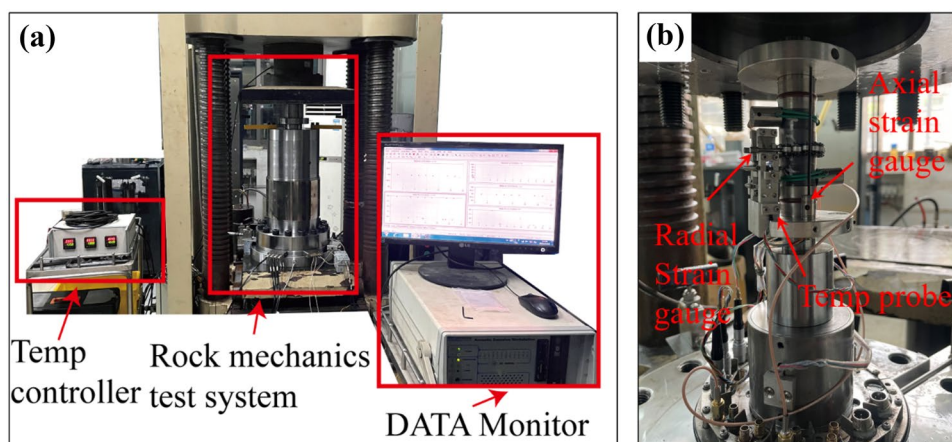
The real-time high temperature triaxial compressive test process mainly includes heating and stress loading. Firstly, put the complete sample into the heat shrinkable tube, use the high temperature hot air gun to make the upper and lower end caps and the sample stereotypes, and check the overall sealing of the sample. The radial and axial strain gages are installed around the sample to ensure proper transmission of sensor signals. Put the sample into the triaxial chamber, install the temperature probe, and inject the hydraulic oil. The sample was heated to the target temperature value at a rate of 2 °C /min through the heating device and kept constant in the triaxial chamber for 2 h to ensure uniform heating of the whole sample. Then confining pressure was then applied to the target value at a loading rate of 0.5 MPa/s. Finally, the axial stress was applied in an axial displacement control mode with a rate of 0.002 mm/s until the sample failure and achieved the residual strength. Data monitor records the data throughout the test.

Main experimental results

Whole-rock mineral content

The XRD result of shale (Fig. 4) shows that the main mineral is quartz, which accounts for more than 67% of the whole rock-mineral content, and the clay mineral content is 18%, which is relatively small, followed by small amounts of Dolomite, Plagioclase K-Feldspar, Calcite, and Pyrite. In general, the Shizhu shale is high in brittle minerals and belongs to the quartz-rich shale category, with good fracability, which is a crucial factor in causing hydraulic fractures to form complex morphologies.
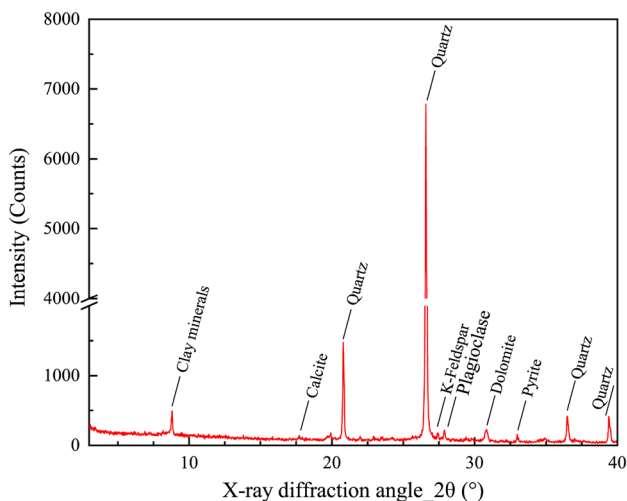

Fig. 4 XRD (X-ray diffraction pattern) result of shale

Mechanical property

The real-time high temperature triaxial stress–strain curve of shale is shown in Fig. 5. It is not difficult to find that most of the stress–strain curves contain 4 stages (compaction stage, elastic stage, yield stage, and residual deformation stage). It is worth noting that the stress–strain curves under uniaxial conditions exhibit good brittle characteristics whether at 25 °C, 80 °C or 150 °C. This is because the linear growth trend of the curve is obvious before the deviatoric stress drop, and no obvious yield point is observed during this process (σ_0 in Fig. 4d). σ_0 is the point at which the rock transitions from elastic to inelastic (Brady and Brown 2006), and the yield stage is the primary characteristic of shale plastic deformation. On the other hand, before the peak deviatoric stress suddenly drops, there is an obvious inflection point in the change rate of radial strain compared with axial strain. At this inflection point, the change rate of radial strain began to increase rather than follow a linear growth trend. This means that the initiation and propagation of fractures parallel to the loading direction is the primary mode of the final failure of the sample, which can be observed in "Failure mode" section (failure mode of the sample). Under triaxial conditions, stress–strain curves show apparent changes, such as a greater rate of the elastic stage curve rise, a longer yield stage, and a slower rate of post-peak curve drop. Although the overall stiffness of the sample becomes larger with the increase of the confining pressure, the sample accumulates more damage before the failure, and part of the work done by the external force is converted into plastic energy inside the sample.

Furthermore, most triaxial stress–strain curves exhibit significantly different yield and residual deformation stages under different temperature conditions. This indicates that most shales have produced varying degrees of plastic deformation. To some extent, temperature changes will affect shale's transition from elastic to plastic. When the bias stress rises further to the peak point, the stress–strain curve undergoes a short drop and flattens out. Under the same confining pressure conditions, the yield stage of the stress–strain curve at 80 °C appears earlier than at 25 °C, and this phenomenon is more obvious at 150 °C. This phenomenon occurs because Mineral particles in shale expand unevenly as temperature rises, which leads to the rapid increase of microcracks, thus leading to the advance propagation of cracks in shale (Lingdong et al. 2021), the plastic deformation of shale is aggravated. In addition, the frequency of stress drops increases but the amplitude of the drop decreases as temperature rises, according to the post-peak stress–strain curve, and the stress in the residual deformation section is also relatively high, and this phenomenon is most significant at 150 °C. This implies that the increase in temperature causes discontinuous
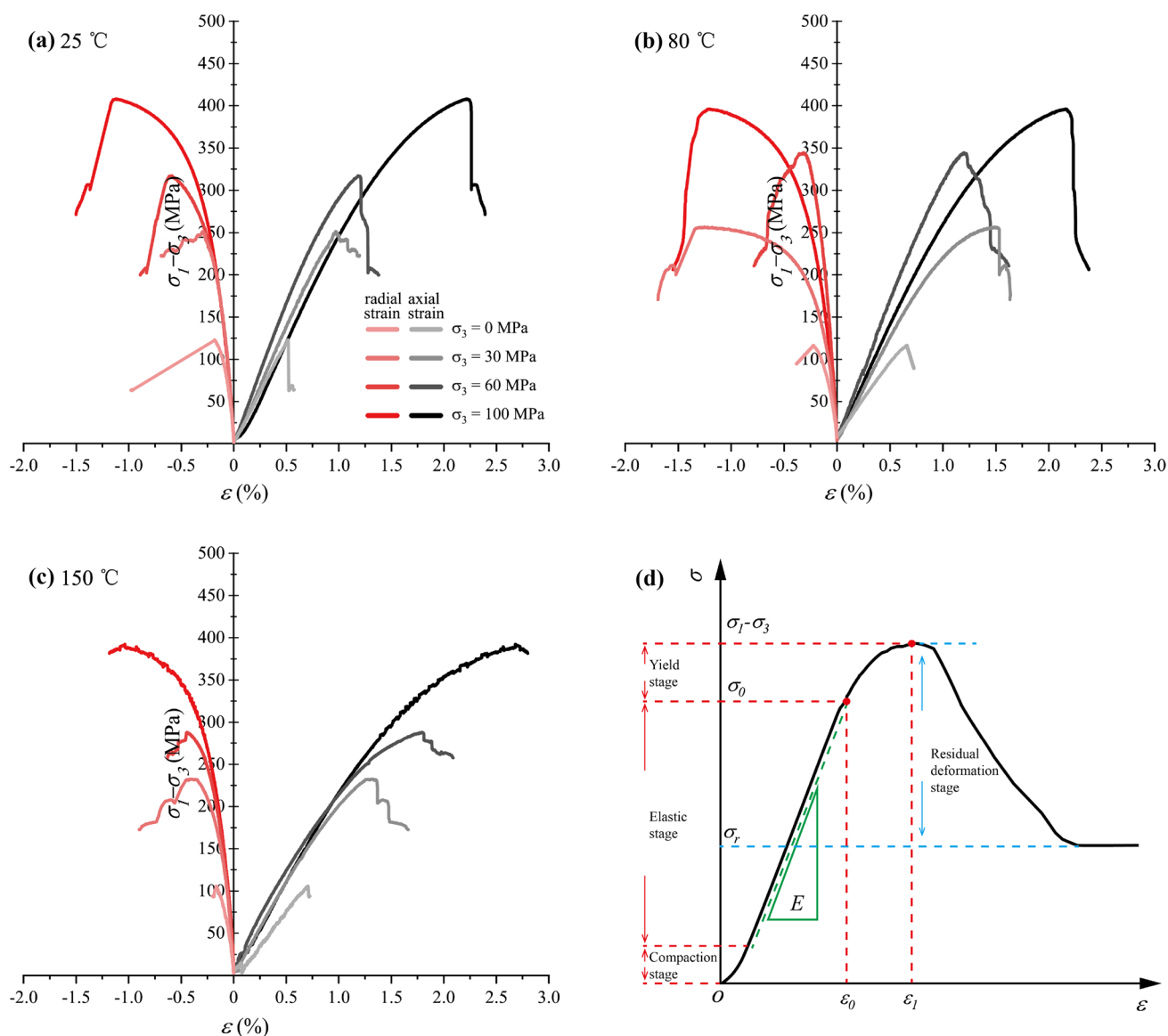
Fig. 5 Stress–strain curves for shale: **a** 25 °C, **b** 80 °C, **c**150°C, **d** Typical stress–strain curve. σ_0: yield stress, $\sigma_1 - \sigma_3$: peak deviatoric stress, σ_r: residual stress, ε_0: yield strain, ε_1: peak strain, E: elastic modulus

rupture of the main surface of rupture, and this discontinuous rupture will increase the frictional strength between the surface of rupture (Guo et al. 2022), resulting in an increase in residual stress. In summary, confining pressure triggers the transition of shale from brittle to plastic, and an increase in temperature exacerbates this process.

The relevant mechanical parameters of shale after real-time high temperature triaxial compressive tests are shown in Fig. 6. For the purpose of analysis, we use room temperature (25 °C) uniaxial ($\sigma_3 = 0$ MPa) shale as a benchmark for evaluating the mechanical properties of high temperature and high stress shale rocks. From Fig. 6a, the peak deviatoric stress ($\sigma_1 - \sigma_3$) of all shales is mostly distributed in the range of 100–410 MPa. At a

certain temperature, as the confining pressure rises, $\sigma_1 - \sigma_3$ of shale generally presents an increasing trend, which is a similar law to what most scholars have found (Chen et al. 2019; Yang et al. 2020; Hu et al. 2021). When the temperature changes, we can find that under the uniaxial condition, $\sigma_1 - \sigma_3$ gradually decreases as the temperature rises. The largest decrease ratio of uniaxial compressive strength of shale at 150 °C relative to 25 °C was 13.7%, while it was only 4.9% at 80 °C. In the triaxial condition, the confining pressure is 30 MPa and 60 MPa, showing a roughly decreasing trend as temperature rises. When the confining pressure reaches 60 MPa, the shale at 150 °C decreased the most, which was 9.2% lower than that of the shale at 25 °C. This is because under the condition of
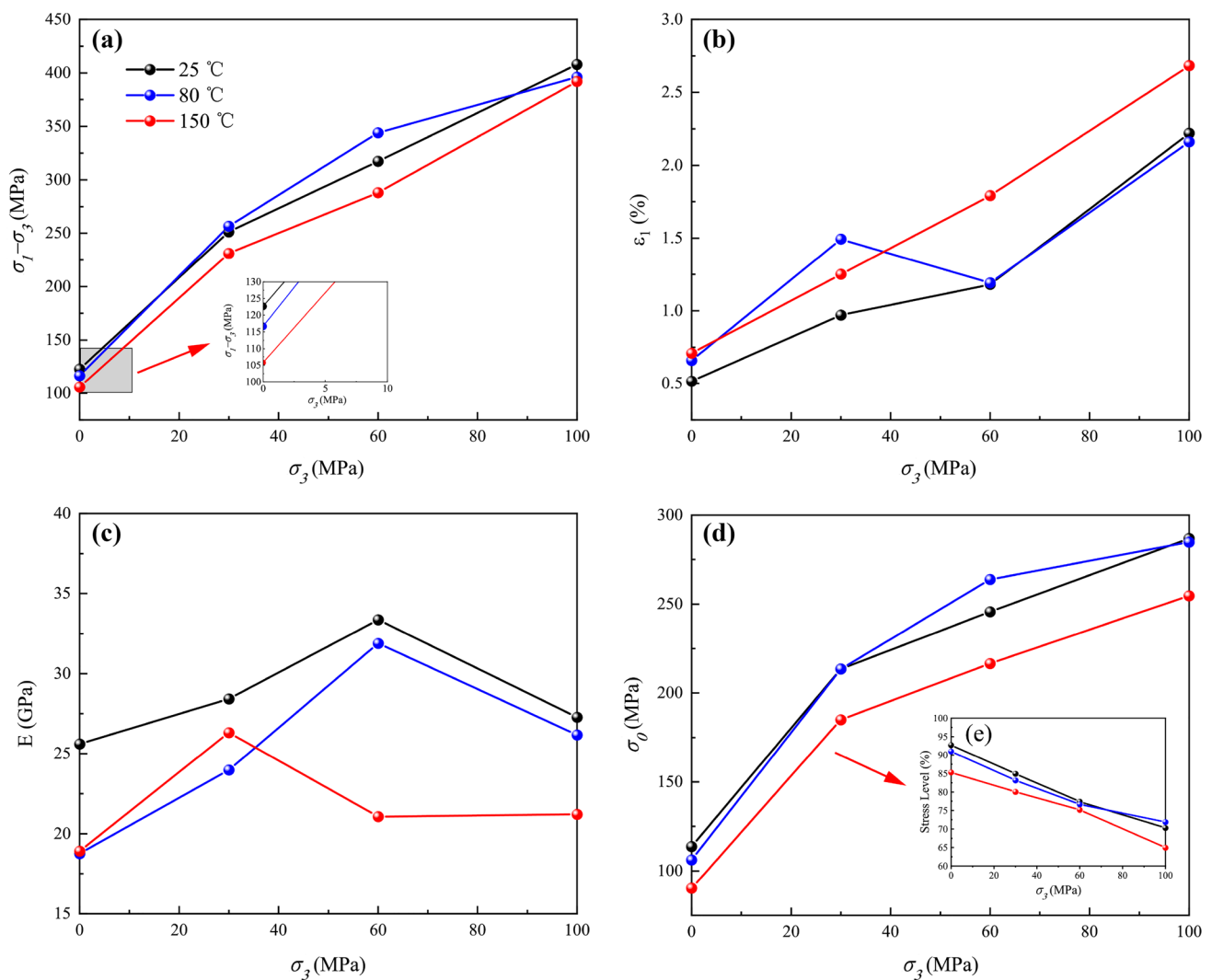
Fig. 6 Mechanical parameters of shale: **a** peak deviatoric stress, **b** peak strain, **c** elastic modulus, **d** yield stress, **e** stress level

medium and low confining pressure, the higher the heating temperature, the more intense the thermal motion of the rock crystal particles, and the cohesion between them is weakened, and the particles are easily displaced, which can induce the appearance of new micro-cracks, thereby enhancing the plastic of the rock, resulting in a decrease in the compressive strength (Suo et al. 2020). However, when the confining pressure comes to 100 MPa, $\sigma_1 - \sigma_3$ does not decrease significantly as the temperature rises. Instead, the difference between $\sigma_1 - \sigma_3$ starts to become smaller. The shale at 150 °C is only 3.9% lower than that at 25 °C. This may be because the high confining pressure will effectively suppress the movement between rock particles induced by temperature. At this time, for the change of compressive strength, the confining pressure occupies the dominant role, and the role of temperature change is no longer significant.

At the peak deviatoric stress, we recorded the corresponding peak strain (ε_1), and the results are shown in Fig. 6b. Obviously, under different temperature conditions, ε_1 generally shows a trend of increasing as the confining pressure rises. When the temperature changes and the confining pressure does not change, we can find that the shale with the $\sigma_3 \leq 60$ MPa, the higher the heating temperature, the higher the value of ε_1. When $\sigma_3 = 100$ MPa, the ε_1 value of shale at 25 °C and 80 °C is roughly similar, which is about 4.2 times that under room temperature uniaxial condition, while the ε_1 value of 150 °C shale will continue to rise, which is 5.2 times that under room temperature uniaxial condition. This means that the change of ε_1 value is only sensitive to high temperature, and is no longer sensitive to medium and low temperature, especially when the confining pressure is high.

At the elastic stage of the stress–strain curve, we calculated the elastic modulus (E) of the shale, and the results are shown in Fig. 6c. At the same temperature, the E generally shows an increasing trend as the confining pressure rises. E distribution of shale at 25 °C and 80 °C is between 18.8 and 33.4 GPa, while that of shale at 150 °C is between 18.9 and 263 GPa. When the confining pressure is constant, the increase in temperature will cause the decrease of E. Among them, 150 °C has the most obvious effect on E. At $\sigma_3 = 60$ MPa, 150 °C decreased by 36.9% relative to 25 °C. This is mainly because as the temperature rises, the pore volume of shale expands and the pore morphology will also change. These changes enhance the deformability and ductility of shale while weakening its own stiffness (Masri et al. 2014).

In addition, we recorded the yield stress (σ_0) of the shale and the stress level relative to $\sigma_1 - \sigma_3$. From Fig. 6d, e, we can see the σ_0 distribution of 25 °C and 80 °C shales ranges from 106 to 287 MPa, at 70–93% of the $\sigma_1 - \sigma_3$ stress level. 150 °C shales have an σ_0 distribution of 90–255 MPa, at 65–85% of the $\sigma_1 - \sigma_3$ stress level. This means that at a certain confining pressure, an increase in temperature will accelerate the transition from elastic to inelastic shale. Among them, the acceleration effect of 150 °C is obvious, and the stress level for plastic deformation is advanced by 7.4% for uniaxial shales and by 5.4% for $\sigma_3 = 100$ MPa shales.

Failure mode

To further clarify the failure mode of the shale, we took photographs of the samples. From Fig. 7, all shales can be divided into three main failure modes: tensile failure, shear failure and tensile-shear composite failure. Under uniaxial conditions, the shales all show a tensile failure mode. At 25 °C, the shale consists mainly of a single main tensile fracture and a few small tensile fractures, and the main fracture is parallel to the loading direction and through the sample. At 80 °C, the shale consists mainly of several medium-sized tensile fractures parallel to each other, making the whole sample split to both sides, resulting in obvious volume expansion. At 150 °C, the shale consists mainly of a single main tensile fracture and local small tensile fractures. Under triaxial conditions, the shale gradually exhibits a shear-dominated failure mode. When the confining pressure reaches 30 MPa, the shale gradually transitions from the composite failure mode of single oblique shear fracture + tensile fracture to the composite failure mode of "V" type shear fracture + tensile fracture as the temperature rises. When the confining pressure is 60 MPa, the shale at 25 °C and 80 °C mainly exhibits the pure shear failure mode of single oblique shear fracture and "V" type shear fracture, while the shale at 150 °C

Fig. 7 Failure morphology of shale
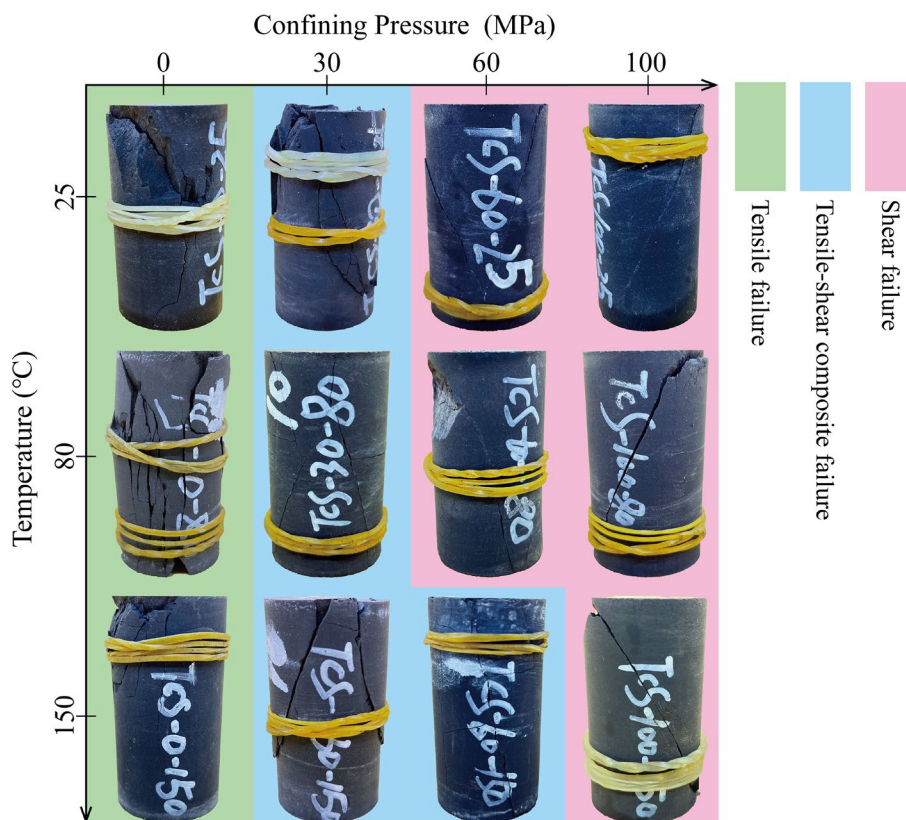
still shows the composite failure mode of single oblique shear fracture + tensile fracture. This is because under low medium confining pressure conditions, high temperatures can effectively weaken the cementation ability between bedding plane or between natural fractures, which can easily open these fractures during shale failure slip, resulting in a multi-fracture failure mode. However, when the confining pressure rises to 100 MPa, the weakening effect of high temperature seems to lose its effect. At this point, all shales exhibit a pure shear failure mode with a single oblique shear fracture and no other fracture opening.

GSI-strength degradation model and statistical damage constitutive model

GSI-strength degradation model

In 1980, E. Hoek and E. T. Brown first proposed Hoek–Brown strength criterion, which can reflect the nonlinear empirical relationship between the maximum principal stresses during rock failure (Hoek and Brown 1980). Over the years, the criterion has formed a more complete system through the continuous development and improvement of a large number of researchers. Undoubtedly, the H-B strength criterion is the most commonly used and influential rock strength criterion. Subsequently, E. Hoek et al. improved the H-B strength criterion in 1992 and named it the generalized H-B strength criterion, which is now more widely used, with the following expressions (Hoek et al. 1992):

$$\sigma_1 = \sigma_3 + \sigma_c \left(m_b \frac{\sigma_3}{\sigma_c} + s \right)^a \tag{1}$$

where σ_1 is the maximum effective principal stress, σ_3 is the minimum effective principal stress, σ_c is the uniaxial compressive strength of intact rock, m_b, s and a are empirical parameters with a scale of 1 that reflect the characteristics of the rock mass, respectively. m_b and a are for different rock masses, and s reflects the degree of rock fragmentation. Subsequently, Hoek et al. (Hoek 1994; Hoek et al. 2000) further introduced the geological intensity index (GSI) and m_i (an empirical parameter with the same scale of 1 as m_b) to determine the values of m_b, s, a:

For rock mass with good quality, GSI > 25.0, there is the following equation (Feng et al. 2018; Zhang et al. 2019).

$$\left. \begin{array}{l} m_b = \exp\left(\dfrac{\text{GSI} - 100}{28}\right) m_i \\[2mm] s = \exp\left(\dfrac{\text{GSI} - 100}{9}\right) \\[2mm] a = 0.5 \end{array} \right\} \tag{2}$$

For intact rock materials, such as shale at 25 °C, the GSI = 100. For rocks that have undergone thermal damage, the weakening of their properties leads us to equate them to non-consecutive rocks (Hou and Peng 2019), whose GSI must decrease. Therefore, to use the H-B strength criterion to describe the variation law of shale strength under high temperature and high stress conditions, it is first necessary to obtain the weakened GSI value. The determination of GSI at different temperatures mainly adopts the following equation.

When $\sigma_3 = 0$ MPa, Eq. 1 can be simplified to:

$$\sigma_1 = \sigma_c \exp\left(\frac{\text{GSI} - 100}{9}\right)^{0.5} \tag{3}$$

In addition, using the uniaxial compressive strength of shale at different temperature conditions:

$$\sigma_1 = \sigma_c(25°C, 80°C, 150°C) \tag{4}$$

The GSI values at different temperatures can be obtained, and the m_i values of shale at different temperature and confining pressure can be fitted by taking them into Eqs. 1, 2. The value of s can be obtained from the GSI value. The curves of GSI-strength degradation model are obtained by combining the data points of different confining pressures under the same temperature condition and using the least squares method to obtain the values of m_i and m_b.

Verification of GSI-strength degradation model

Figure 8 demonstrates the variation law of the peak stress with the confining pressure described based on the GSI-Strength degradation model. It is obvious that the shale strength envelope under different temperature
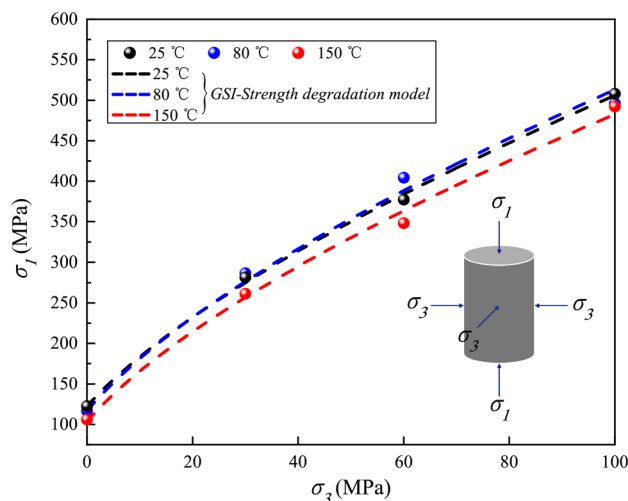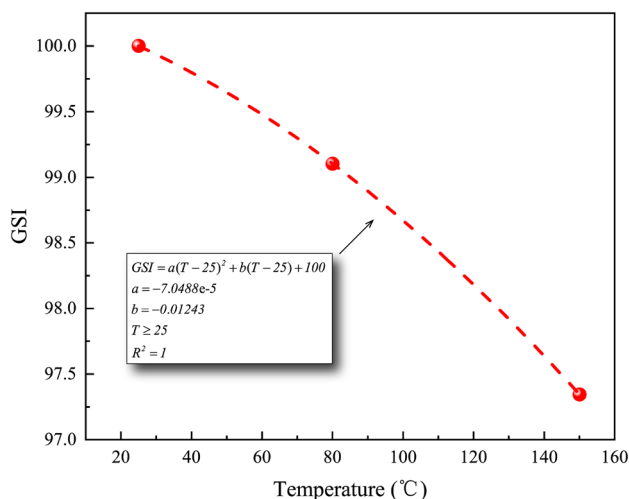

Fig. 8 GSI-Strength degradation model fitting curve

Table 2 Main parameters of GSI-Strength degradation model

Temp °C	σ_c MPa	GSI	M_i	M_b	s	GSI-strength degradation model	R^2
25	122.7	100.00	12.22	12.22	1.00	$\sigma_1 = \sigma_3 + \sigma_{c(25°C)}\left(12.22\sigma_3/\sigma_{c(25°C)} + 1\right)^{0.5}$	0.999
80	116.7	99.10	14.07	13.63	0.91	$\sigma_1 = \sigma_3 + \sigma_{c(25°C)}\left(13.63\sigma_3/\sigma_{c(25°C)} + 0.91\right)^{0.5}$	0.992
150	105.8	97.34	12.17	11.07	0.74	$\sigma_1 = \sigma_3 + \sigma_{c(25°C)}\left(11.07\sigma_3/\sigma_{c(25°C)} + 0.74\right)^{0.5}$	0.995

$GSI = a(T - 25)^2 + b(T - 25) + 100$
$a = -7.0488e{-}5$
$b = -0.01243$
$T \geq 25$
$R^2 = 1$

Fig. 9 Fitted curve of GSI with temperature

conditions exhibits a significant nonlinearity, which is in good accordance with the experimental data. This indicates that the GSI-Strength degradation model can better characterize the variation law of shale strength under different temperature and confining pressure conditions compared with other linear models. The main parameters of the GSI-Strength degradation model are shown in Table 2. It can be seen that the GSI value and s value gradually decrease with increasing temperature. The correlation coefficients of the GSI-strength deterioration models for 25 °C, 80 °C and 150 °C are all greater than 0.99. In addition, the GSI value has a good nonlinear relationship with temperature. Therefore, it seems more reasonable to fit it with a quadratic polynomial. Since the damage degree of shale is low under medium and low temperature conditions, the damage degree of shale is greatly increased under high temperature conditions. The higher the temperature, the faster the shale strength degradation. The specific fitting results are shown in Fig. 9. Finally, we bring the fitting results into Eqs. 1, 2 to get the GSI-strength degradation model based on the H-B strength criterion.

Damage constitutive model based on GSI-strength degradation model

In this section, combined with the GSI-strength degradation model under high temperature and high stress conditions in the previous section, the statistical damage constitutive model of shale is derived by introducing the Weibull distribution. The solved model parameters and total damage variables are used to characterize the fine-scale damage evolution of the shale, predict its macroscopic deformation damage law, and validate it using experimental data.

According to the strain equivalence theory and effective stress principle proposed by Lemaitre (Lemaitre 1985), the relationship between nominal stress A and effective stress C can be expressed as:

$$[\sigma] = [\sigma^*](1 - [D]) \tag{5}$$

where $[\sigma]$ is the nominal stress matrix, $[\sigma^*]$ is the effective stress matrix, and $[D]$ is the damage matrix, respectively. From Eq. 5, it can be seen that $D = 1$ when $[\sigma] = 0$, at which point the rock is in a state of complete failure. However, laboratory tests show that under triaxial conditions, the stress does not drop completely to 0 when it reaches its peak, but instead there is a residual stress σ_r due to the frictional strength of the rupture surface. Thus, the nominal stress can be composed of the residual stress σ_r provided by the damaged part of the rock and the effective stress σ^* provided by the undamaged part (Zhang et al. 2020; Chen et al. 2021), Eq. 5 can be rewritten in the following form:

$$\sigma_1 = \sigma_1^*(1 - D) + \sigma_r D \tag{6}$$

In addition, the stress tested by laboratory rock mechanics tests is generally deviatoric stress, and to conform to the stress–strain curve of the actual test, Eq. 6 can be further rewritten as:

$$\sigma_1 - \sigma_3 = \left(\sigma_1^* - \sigma_3^*\right)(1 - D) + \left(\sigma_r - \sigma_3^*\right)D \tag{7}$$

The damage accumulated by the micro unit will cause the degradation of rock properties and result in rock damage. Therefore, D can be expressed as the ratio of the number of

accumulated damages of micro units (N_d) to the total number of micro units (N) as the following equation:

$$D = \frac{N_d}{N} \tag{8}$$

For the applicability of the constitutive model and we can get a clearer understanding of the relationship between the model parameters, the following assumptions need to be stated in advance:

(1) The damage to the rock is homogeneous.
(2) Rock microunits strictly conform to Hooke's law before damage. The damage of undamaged microunits is instantaneous and yielding satisfies the H-B strength criterion (Eqs. 1, 2).
(3) Heat transfer in rocks is carried out only in the form of heat conduction, and heat transfer in the form of convection and radiation is not considered.
(4) The rocks are microscopically joined by random non-homogeneous particles and the strength of the micro units conforms to the Weibull distribution.

Also, we introduce the Weibull distribution (Eq. 9) and bring Eq. 8 into Eq. 9 to obtain Eq. 10. Based on assumption (2) we can also obtain Eq. 11.

$$N_d = \int_0^{f_{HB}} N \frac{\gamma}{\beta} \left(\frac{x}{\beta} \right)^{\gamma-1} \exp\left[-\left(\frac{x}{\beta} \right)^{\gamma} \right] dx \tag{9}$$

$$D = 1 - \exp\left[-\left(\frac{f_{HB}(\sigma^*)}{\beta} \right)^{\gamma} \right] \tag{10}$$

$$\sigma_1^* - \sigma_3^* = E\varepsilon_1^* \tag{11}$$

where E is the modulus of elasticity of the rock, and ε_1^* is the effective strain, γ and β are Weibull distribution parameters, respectively.

From the laboratory test data, we can see that the radial strain of the rock is much smaller than the axial strain. We can assume that the damage of the rock occurs mainly in the axial direction and the radial damage is neglected, so we have $\sigma_2^* = \sigma_2$ and $\sigma_3^* = \sigma_3$. The effective strain (ε_1^*) can be equated to the axial strain (ε_1) by the coordination of deformation

between rock micro units. Combining Eqs. 7, 10 and 11, we obtain Eq. 12. At the same time, $f_{HB}(\sigma^*)$ can be expressed as an invariant of the effective stress tensor of the following form (Eq. 13) (Ma et al. 2020), whereupon $f_{HB}(\sigma^*)$ can be further expressed as Eq. 14.

$$\sigma_1 - \sigma_3 = \left[E\varepsilon_1 - (\sigma_r - \sigma_3) \right] \exp\left[-\left(\frac{f_{HB}(\sigma^*)}{\beta} \right)^{\gamma} \right] + (\sigma_r - \sigma_3) \tag{12}$$

$$f_{HB}(\sigma^*) = \sigma_c m_i \frac{I_1^*}{3} + 3J_2^* + \frac{2}{3}\sqrt{3}\sigma_c m_i \sqrt{J_2^*} \tag{13}$$

$$f_{HB}(\sigma^*) = \sigma_c m_i E\varepsilon_1 + (E\varepsilon_1 - \sigma_3)^2 \tag{14}$$

where $I_1^* = \sigma_1^* + \sigma_2^* + \sigma_3^*$ is the first invariant of the effective stress tensor, $J_2^* = \frac{1}{6}\left[(\sigma_1^* - \sigma_2^*)^2 + (\sigma_1^* - \sigma_3^*)^2 + (\sigma_2^* - \sigma_3^*)^2 \right]$ is the second invariant of the partial effective stress tensor, respectively. σ_c and m_i can be obtained from the parameters obtained by the GSI-Strength degradation model in Table 2, so that the degradation effect of high temperature on rock properties can be reflected in the statistical damage constitutive model.

Combined with the geometric conditions of the shale stress–strain curve (Fig. 4), it can be known that (1) $\sigma_1 - \sigma_3 = \sigma_p, \varepsilon_1 = \varepsilon_p$ and (2) $\sigma_1 - \sigma_3 = \sigma_p, d\sigma_p/d\varepsilon_p = 0$. Bringing in the boundary conditions, the partial derivative of Eq. 12 can be obtained as follows:

$$\left(\frac{f_{HB}(\sigma_p^*)}{\beta} \right)^{\gamma} = \frac{f_{HB}(\sigma_p^*)}{\gamma\left(E\varepsilon_p - (\sigma_r - \sigma_3) \right)\left(\sigma_c m_i + 2E\varepsilon_p - 2\sigma_3 \right)} \tag{15}$$

By simultaneous Eqs. 12 and 15, the parametric expressions can be derived as:

$$\gamma = \frac{f_{HB}(\sigma_p^*)}{\left(E\varepsilon_p - (\sigma_r - \sigma_3) \right)\left(\sigma_c m_i + 2E\varepsilon_p - 2\sigma_3 \right) \ln \frac{E\varepsilon_p - (\sigma_r - \sigma_3)}{\sigma_p - \sigma_r}} \tag{16}$$

Table 3 Constitutive model parameter value under different temperature confining pressure conditions

Sample no	$\sigma_1 - \sigma_3$ MPa	ε_p %	E MPa	$\sigma_r - \sigma_3$ MPa	σ_c MPa	m_i 1	γ 1	β 10^3
TCS-0-25	122.7	0.517	25,610	69.0	122.7	12.22	11.69	251.912
TCS-30-150	231.2	1.250	26,324	178.9	105.8	12.17	1.72	497.588
TCS-60-150	288.1	1.791	21,072	262.6	105.8	12.17	1.77	465.848
TCS-100-150	392.1	2.682	21,213	100.0	105.8	12.17	1.93	140.402
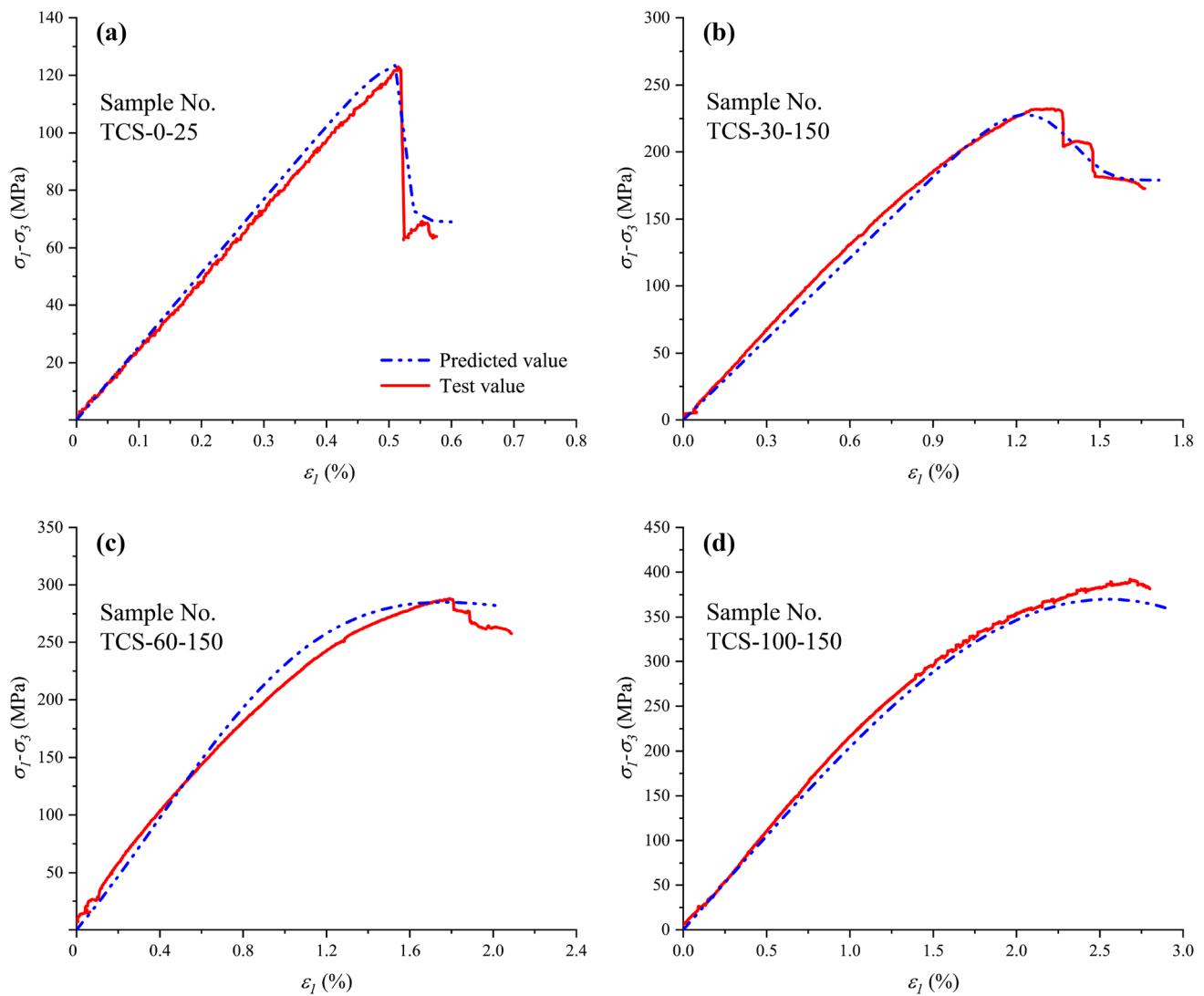
Fig. 10 Comparison of test curves and constitutive model curves: **a** $\sigma_3 = 0$ MPa Temperature = 25 °C, **b** $\sigma_3 = 30$ MPa Temperature = 150 °C, **c** $\sigma_3 = 60$ MPa Temperature = 150 °C, **d** $\sigma_3 = 100$ MPa Temperature = 150 °C

$$\beta = \frac{f_{\mathrm{HB}}\left(\sigma_{\mathrm{p}}^{*}\right)}{\ln\left(\frac{E\varepsilon_{\mathrm{p}} - \left(\sigma_{\mathrm{r}} - \sigma_{3}\right)}{\sigma_{\mathrm{p}} - \sigma_{\mathrm{r}}}\right)^{\frac{1}{\gamma}}} \tag{17}$$

Verification of damage constitutive model

By selecting the stress–strain curves and related mechanical parameters of some shale in "Mechanical property" and "Verification of GSI-strength degradation model" sections, the model parameters in the damage constitutive model can be obtained. The detailed results are shown in Table 3. Combined with the model parameters, we compared the experimental curve and the model prediction curve, and the comparison of the two curves is shown in Fig. 9.

The actual test and model prediction curves in Fig. 10 have a high degree of matching. This shows that the statistical damage constitutive model based on the GSI-strength degradation model established in this paper can effectively reflect real-time high temperature shale deformation characteristics during stress loading. Although the stress drop characteristics at post-peak of the stress–strain curve are not very obvious in the model prediction curve, the peak stress and peak strain calculated by the effective stress principle are basically consistent with actual test data. In general, the model can reflect the failure law of rock under thermal–mechanical coupling to a certain extent.

Discussion

Although the improved GSI-strength degradation model based on the H-B strength criterion can be used to characterize the change of rock strength under the coupled thermal–mechanical coupling effect, the derived statistical damage constitutive model still has certain limitations. There are two main points: 1. It is not difficult to see from Eq. 12 that the damage constitutive model is mainly related to the residual strength and elastic modulus of the rock. Therefore, when selecting experimental data to check the model's validity, data with obvious strain characteristics at pre-peak and post-peak should be selected. 2. The assumptions used to derive the model mean the model has certain limitations, so the model can only be applied when the rock material meets these conditions. Consequently, to maximize the practical usefulness of the damage constitutive model, the above deficiencies need to be further improved and refined in future research work.

Even though the GSI-strength degradation model and the constitutive model cannot 100% predict the mechanical properties of rocks and describe the stress–strain curve of the whole process, they still do not affect their application in engineering practice. Especially when basic rock mechanics data is needed to optimize hydraulic fracturing stimulation parameters, but it is difficult to obtain downhole cores and the experimental environment of formation temperature and stress are difficult to achieve, the above model is undoubtedly an effective tool for predicting rock mechanical properties. Overall, the research results of this paper are enlightening for solving the difficult problems encountered in the development of deep shale gas.

Summary and conclusions

In this paper, the lower Silurian Longmaxi Formation shale is taken as the research object, real-time high temperature and high stress triaxial compression tests were conducted, and GSI-strength degradation and constitutive models were derived. The main conclusions are as follows:

(1) The temperature increase will lead to a maximum decrease of 13.7% in peak deviatoric stress, a maximum decrease of 36.9% in elastic modulus, a maximum increase of 140% in peak strain, and a maximum advance of 7.4% in yield stress level. Under high confining pressure, peak strain and elastic modulus are only sensitive at 150 °C

(2) Under the condition of low confining pressure, high temperature can effectively affect the failure mode of shale. As the confining pressure increases, the shale will change from the multi-fracture tensile-shear composite failure mode to a single shear fracture failure mode, and the effect of temperature on the failure mode is not obvious anymore. The confining pressure will trigger the transition from brittle to plastic shale, and the increase in temperature will accelerate this process.

(3) The proposed GSI-Strength degradation model can characterize the variation law of shale strength with confining pressure and better describe the nonlinear characteristics exhibited by the strength envelope.

(4) The shale statistical damage constitutive model is in excellent agreement with the actual stress–strain curve and can fully reflect the shale deformation and failure characteristics under deep formation conditions.

Declarations

Conflict of interest The authors declare that they have no known competing financial interests or personal relationships that could have appeared to influence the work reported in this paper.

Ethics approval All ethical requirements of the journal are met. This article does not contain any studies with human participants or animals performed by any of the authors.

Consent to participate All authors agree to be the author of the publication.

Consent for publication All authors agree to submit their publications to this journal.

References

Al-Fatlawi OF (2018) Numerical Simulation for the Reserve Estimation and Production Optimization from Tight Gas Reservoirs. Curtin University, Perth

Brady BHG, Brown ET (2006) Rock Mechanics for underground mining, 3rd edn. Springer, Berlin

Chen Y, Jiang C, Yin G et al (2019) Permeability evolution under true triaxial stress conditions of Longmaxi shale in the Sichuan Basin, Southwest China. Powder Technol 354:601–614. https://doi.org/10.1016/j.powtec.2019.06.044

Chen Y, Lin H, Wang Y et al (2021) Statistical damage constitutive model based on the Hoek-Brown criterion. Arch Civ Mech Eng 21:1–9. https://doi.org/10.1007/s43452-021-00270-y

Department of Energy (2012) Hydraulic Fracturing Technology. https://www.energy.gov/fecm/hydraulic-fracturing-technology

Duan H, Li H, Dai J et al (2019) Horizontal well fracturing mode of "increasing net pressure, promoting network fracture and keeping conductivity" for the stimulation of deep shale gas reservoirs: a case study of the Dingshan area in SE Sichuan Basin. Nat Gas Ind B 6:497–501. https://doi.org/10.1016/j.ngib.2019.02.005

Fan X, Luo N, Liang H et al (2021) Dynamic breakage characteristics of shale with different bedding angles under the different ambient temperatures. Rock Mech Rock Eng 54:3245–3261. https://doi.org/10.1007/s00603-021-02463-6

Feng W, Dong S, Wang Q et al (2018) Improving the Hoek–Brown criterion based on the disturbance factor and geological strength index quantification. Int J Rock Mech Min Sci 108:96–104. https://doi.org/10.1016/j.ijrmms.2018.06.004

Guo Y, Huang L, Li X et al (2020) Experimental investigation on the effects of thermal treatment on the physical and mechanical properties of shale. J Nat Gas Sci Eng 82:103496. https://doi.org/10.1016/j.jngse.2020.103496

Guo W, Guo Y, Yang C et al (2022) Experimental investigation on the effects of heating-cooling cycles on the physical and mechanical properties of shale. J Nat Gas Sci Eng 97:104377. https://doi.org/10.1016/j.jngse.2021.104377

Han K, Song X, Yang H (2021) The pricing of shale gas: a review. J Nat Gas Sci Eng. https://doi.org/10.1016/j.jngse.2021.103897

He X, Li W, Dang L et al (2021) Key technological challenges and research directions of deep shale gas development. Nat Gas Ind 41:118–124. https://doi.org/10.3787/j.issn.1000-0976.2021.01.010

Hoek E (1994) Strength of rock and rock masse. Int Soc Rock Mech News J 2:4–16

Hoek E, Brown ET (1980) Empirical strength criterion for rock masses. J Geotech Eng Div 106:1013–1035

Hoek E, Wood D, Shah S (1992) A modified Hoek-Brown failure criterion for jointed rock masses. In: Proceedings of rock characteristics ISRM, pp 209–214

Hoek E, Kaiser PK, Bawden WF (2000) Support of underground excavations in hard rock. CRC Press, Boca Raton

Hou D, Peng J (2019) Triaxial mechanical behavior and strength model for thermally-damaged marble. J Rock Mech Eng 38:2603–2613. https://doi.org/10.13722/j.cnki.jrme.2017.1656

Hu J, Gao C, Xie H et al (2021) Anisotropic characteristics of the energy index during the shale failure process under triaxial compression. J Nat Gas Sci Eng 95:104219. https://doi.org/10.1016/j.jngse.2021.104219

ISRM (1984) Suggested methods for determining the strength of rock materials in triaxial compression: revised version: ISRM Comm on Standardization of Laboratory and Field-Tests Int J Rock Mech Min SciV20, N6, Dec 1983, P283–290. Int J Rock Mech Min

Sci Geomech Abstr 21:46. https://doi.org/10.1016/0148-9062(84)91226-9

Jiang T, Bian X, Wang H et al (2017) Volume fracturing of deep shale gas horizontal wells. Nat Gas Ind 37:90–96. https://doi.org/10.3787/j.issn.1000-0976.2017.01.011

Jiang H-P, Jiang A-N, Yang X-R (2021) Statistical damage constitutive model of high temperature rock based on Weibull distribution and its verification. Yantu Lixue/Rock Soil Mech 42:1894–1902. https://doi.org/10.16285/j.rsm.2020.1461

Lemaitre J (1985) A continuous damage mechanics model for ductile fracture. J Eng Mater Technol 107:83–89. https://doi.org/10.1115/1.3225775

Li Y (2021) Mechanics and fracturing techniques of deep shale from the Sichuan Basin, SW China. Energy Geosci 2:1–9. https://doi.org/10.1016/j.engeos.2020.06.002

Li S, Zhou Z, Nie H et al (2022) Distribution characteristics, exploration and development, geological theories research progress and exploration directions of shale gas in China. China Geol 5:110–135. https://doi.org/10.1016/S2096-5192(22)00090-8

Liang X, Xu Z, Zhang J et al (2020) Key efficient exploration and development technoloiges of shallow shale gas: a case study of Taiyang anticline area of Zhaotong National Shale Gas Demonstration Zone. Shiyou Xuebao/acta Pet Sin. https://doi.org/10.7623/syxb202009001

Lingdong L, Xiaoning Z, Ruiqing M et al (2021) Mechanical properties of shale under the coupling effect of temperature and confining pressure. Chem Technol Fuels Oils 57:841–846. https://doi.org/10.1007/s10553-021-01314-y

Liu D, He M, Cai M (2018) A damage model for modeling the complete stress–strain relations of brittle rocks under uniaxial compression. Int J Damage Mech 27:1000–1019. https://doi.org/10.1177/1056789517720804

Liu D, Wang S, Ke X et al (2020a) Mechanical characteristics and factors controlling brittleness of organic-rich continental shales. J Pet Sci Eng 194:107464. https://doi.org/10.1016/j.petrol.2020.107464

Liu L, Ji H, Elsworth D et al (2020b) Dual-damage constitutive model to define thermal damage in rock. Int J Rock Mech Min Sci 126:104185. https://doi.org/10.1016/j.ijrmms.2019.104185

Liu W, Dan Z, Jia Y, Zhu X (2020c) On the statistical damage constitutive model and damage evolution of hard rock at high-temperature. Geotech Geol Eng 38:4307–4318. https://doi.org/10.1007/s10706-020-01296-4

Liu Y-Y, Ma X-H, Zhang X-W et al (2021) A deep-learning-based prediction method of the estimated ultimate recovery (EUR) of shale gas wells. Pet Sci 18:1450–1464. https://doi.org/10.1016/j.petsci.2021.08.007

Long S, Feng D, Li F, Du W (2018) Prospect analysis of the deep marine shale gas exploration and development in the Sichuan Basin, China. J Nat Gas Geosci 3:181–189. https://doi.org/10.1016/j.jnggs.2018.11.001

Ma L, Li Z, Wang M et al (2020) Applicability of a new modified explicit three-dimensional Hoek–Brown failure criterion to eight rocks. Int J Rock Mech Min Sci 133:104311. https://doi.org/10.1016/j.ijrmms.2020.104311

Ma X, Wang H, Zhou S et al (2021) Deep shale gas in China: Geological characteristics and development strategies. Energy Rep 7:1903–1914. https://doi.org/10.1016/j.egyr.2021.03.043

Masri M, Sibai M, Shao JF, Mainguy M (2014) Experimental investigation of the effect of temperature on the mechanical behavior of Tournemire shale. Int J Rock Mech Min Sci 70:185–191. https://doi.org/10.1016/j.ijrmms.2014.05.007

Mohamadi M, Wan RG (2016) Strength and post-peak response of Colorado shale at high pressure and temperature. Int J Rock Mech Min Sci 84:34–46. https://doi.org/10.1016/j.ijrmms.2015.12.012

Qi SZ, Tan XH, Li XP et al (2021) Numerical simulation and experimental verification studies on a unified strength theory-based elastoplastic damage constitutive model of shale. Nat Gas Ind B 8:267–277. https://doi.org/10.1016/j.ngib.2021.04.005

Sadeq D, Al-Fatlawi O, Iglauer S, et al (2020) Hydrate equilibrium model for gas mixtures containing methane, nitrogenand carbon dioxide. In: Proceedings of the annual offshore technology conference

Suo Y, Chen Z, Rahman SS (2020) Changes in shale rock properties and wave velocity anisotropy induced by increasing temperature. Nat Resour Res 29:4073–4083. https://doi.org/10.1007/s11053-020-09693-5

Vishal V, Rizwan M, Mahanta B et al (2022) Temperature effect on the mechanical behaviour of shale: implication for shale gas production. Geosyst Geoenviron 1:100078. https://doi.org/10.1016/j.geogeo.2022.100078

Wan C, Song Y, Li Z et al (2022) Variation in the brittle-ductile transition of Longmaxi shale in the Sichuan Basin, China: the significance for shale gas exploration. J Pet Sci Eng 209:109858. https://doi.org/10.1016/j.petrol.2021.109858

Wang Z, Liu M, Guo H (2017) A strategic path for the goal of clean and low-carbon energy in China. Nat Gas Ind B 3:305–311

Wang ZL, Shi H, Wang JG (2018) Mechanical behavior and damage constitutive model of granite under coupling of temperature and dynamic loading. Rock Mech Rock Eng 51:3045–3059. https://doi.org/10.1007/s00603-018-1523-0

Wang L, Guo Y, Zhou X et al (2022) Mechanical properties of marine shale and its roof and floor considering reservoir preservation and stimulation. J Pet Sci Eng 211:110194. https://doi.org/10.1016/j.petrol.2022.110194

Wu X, Huang Z, Li R et al (2018) Investigation on the damage of high-temperature shale subjected to liquid nitrogen cooling. J Nat Gas Sci Eng 57:284–294. https://doi.org/10.1016/j.jngse.2018.07.005

Xing Y, Zhang G, Li S (2020) Thermoplastic constitutive modeling of shale based on temperature-dependent Drucker-Prager plasticity. Int J Rock Mech Min Sci 130:104305. https://doi.org/10.1016/j.ijrmms.2020.104305

Xu XL, Karakus M, Gao F, Zhang ZZ (2018) Thermal damage constitutive model for rock considering damage threshold and residual strength. J Cent South Univ 25:2523–2536. https://doi.org/10.1007/s11771-018-3933-2

Yang S-Q, Yin P-F, Li B, Yang D-S (2020) Behavior of transversely isotropic shale observed in triaxial tests and Brazilian disc tests. Int J Rock Mech Min Sci 133:104435. https://doi.org/10.1016/j.ijrmms.2020.104435

Yang S, Yang D, Kang Z (2021) Experimental investigation of the anisotropic evolution of tensile strength of oil shale under real-time high-temperature conditions. Nat Resour Res 30:2513–2528. https://doi.org/10.1007/s11053-021-09848-y

Ye Q, He X, Suo Y et al (2022) The statistical damage constitutive model of longmaxi shale under high temperature and high pressure. Lithosphere 2022:2503948. https://doi.org/10.2113/2022/2503948

Yi-Sheng L, Zheng-Ping Z, Ren-Fang P et al (2022) Brittleness evaluation of Wufeng and Longmaxi Formation high-quality shale reservoir in southeast of Chongqing. Environ Earth Sci 81:1–9. https://doi.org/10.1007/s12665-022-10274-3

Zeng Y, Chen Z, Bian X (2016) Breakthrough in staged fracturing technology for deep shale gas reservoirs in SE Sichuan Basin and its implications. Nat Gas Ind 36:61–67. https://doi.org/10.3787/j.issn.1000-0976.2016.01.007

Zhang Y, Liu X, Liu X et al (2019) Numerical characterization for rock mass integrating GSI/Hoek–Brown system and synthetic rock mass method. J Struct Geol 126:318–329. https://doi.org/10.1016/j.jsg.2019.06.017

Zhang H, Meng X, Yang G (2020) A study on mechanical properties and damage model of rock subjected to freeze-thaw cycles and confining pressure. Cold Reg Sci Technol 174:103056. https://doi.org/10.1016/j.coldregions.2020.103056

Zhang L, He X, Li X et al (2022a) Shale gas exploration and development in the Sichuan Basin: progress, challenge and countermeasures. Nat Gas Ind B 9:176–186. https://doi.org/10.1016/j.ngib.2021.08.024

Zhang Y, Zhang F, Yang K, Cai Z (2022b) Effects of real-time high temperature and loading rate on deformation and strength behavior of granite. Geofluids 2022:9426378. https://doi.org/10.1155/2022/9426378

Zhao G, Chen C, Yan H (2019) A thermal damage constitutive model for oil shale based on weibull statistical theory. Math Probl Eng 2019:4932586. https://doi.org/10.1155/2019/4932586

Zou C, Zhao Q, Cong L et al (2021) Development progress, potential and prospect of shale gas in China. Nat Gas Ind 41:1–14. https://doi.org/10.3787/j.issn.1000-0976.2021.01.001